ACS APPLIED MATERIALS & INTERFACES

Research Article

www.acsami.org

Constructed Uninterrupted Charge-Transfer Pathways in Three-Dimensional Micro/Nanointerconnected Carbon-Based Electrodes for High Energy-Density Ultralight Flexible Supercapacitors

Yongmin He,*[,†,‡] Wanjun Chen,[†,‡] Jinyuan Zhou,[‡] Xiaodong Li,[‡] Pengyi Tang,[§] Zhenxing Zhang,[‡] Jiecai Fu,[‡] and Erqing Xie*[,‡]

[‡]School of Physical Science and Technology and [§]College of Chemistry and Chemical Engineering, Lanzhou University, Lanzhou 730000, Gansu, P.R. China

Supporting Information

ABSTRACT: A type of freestanding three-dimensional (3D) micro/nanointerconnected structure, with a conjunction of microsized 3D graphene networks, nanosized 3D carbon nanofiber (CNF) forests, and consequently loaded MnO_2 nanosheets, has been designed as the electrodes of an ultralight flexible supercapacitor. The resulting 3D graphene/CNFs/MnO_2 composite networks exhibit remarkable flexibility and highly mechanical properties due to good and intimate contacts among them, without current collectors and binders. Simultaneously, this designed 3D micro/nanointerconnected structure can provide an uninterrupted double charges freeway network for both electron and electrolyte ion to minimize electron accumulation and ion-diffusing resistance, leading to an excellent electrochemical performance. The ultrahigh specific capacitance of 946 F/g from cyclic voltammetry (CV) (or 920 F/g from galvanostatic charging/discharging (GCD)) were obtained, which is superior to that of the present electrode materials based on 3D graphene/MnO_2 hybrid structure (482 F/g). Furthermore, we have also investigated the superior electrochemical performances of an asymmetric supercapacitor device (weight of less than 12 mg/cm^2 and thickness of ~0.8 mm), showing a total capacitance of 0.33 F/cm^2 at a window voltage of 1.8 V and a maximum energy density of 53.4 W h/kg for driving a digital clock for 42 min. These inspiring performances would make our designed supercapacitors become one of the most promising candidates for the future flexible and lightweight energy storage systems.

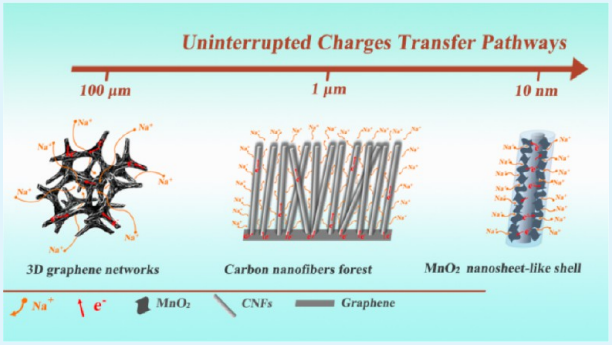

KEYWORDS: *3D micro/nanointerconnected structure, uninterrupted charges transfer pathways, flexible, ultralight, supercapacitors*

INTRODUCTION

Due to their potential applications in portable electronic devices, such as flexible displays, electronic papers, wearable electronics, mobile phones, and portable computers, flexible energy storage devices have attracted more and more attention.[1−4] In particular, flexible supercapacitors have been considered as one of the most promising ones due to their irreplaceable properties, such as fast charging/discharging rate, long life-cycles, high power density, and simple device configuration.[5−7] In view of the flexible supercapacitors' electrode materials, porous carbon materials, showing superior mechanical and electrical properties, low-cost, and excellent capacitance performance with conductive double layers, have been frequently employed.[8−10] Recently, to achieve fundamental investigation into the electrode kinetic process and the relationship between carbon porous structure and electrolyte ions,[11−13] extensive attention has been fixed on the design and fabrication of three-dimensional (3D) multifunctional carbon structures for high-performance supercapacitors.[14−17] Most importantly, those types of 3D carbon materials like porous structures can provide fast transport channels for easy ion access to the solid-state electrode and well-interconnected wall structures for a continuous electron pathway. Thus, it is expected that the flexible supercapacitors with 3D carbon electrodes would show an enhanced electrochemical performance.

Among those 3D carbon structures, nanosized carbon materials have attracted intense attention, including active carbon (AC),[18] carbide-derived carbon,[19] templated mesoporous carbons,[20] and carbon nanotubes (CNTs),[21] carbon nanofibers (CNFs),[22] graphene nanosheets,[23] and their hybrid-based nanostructures.[24−26] The typical advantages inherited from those 3D nanostructured materials include the following:[14,27] (1) large specific surface area (SSA), which can significantly enlarge the electrode/electrolyte contact area per unit mass, and provide more ion adsorption sites for double-

Received: September 11, 2013
Accepted: December 10, 2013
Published: December 10, 2013

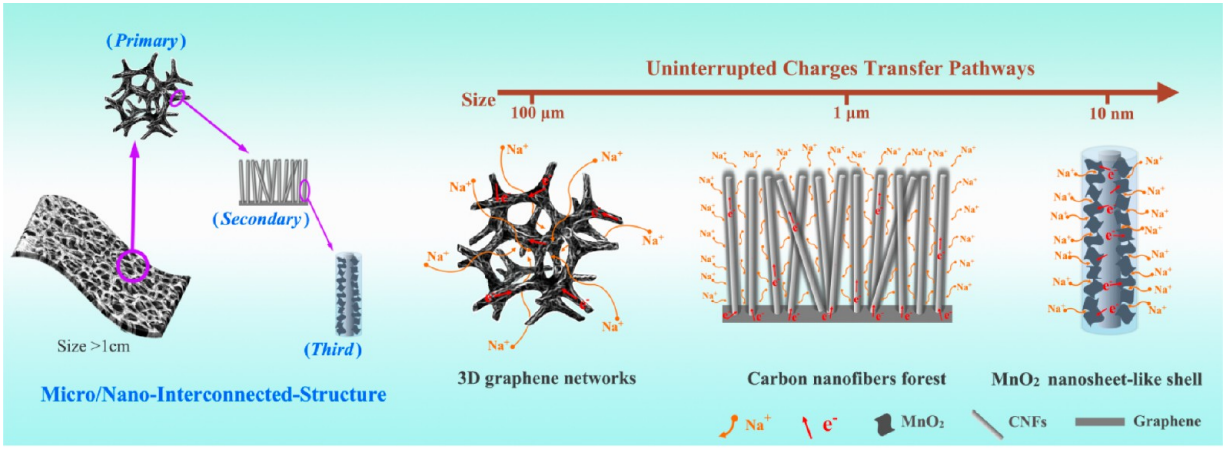

Figure 1. Schematic illustration of 3D micro/nanointerconnected structure as flexible supercapacitor electrode. The designed 3D micro/nanointerconnected structure is based on the bulk hierarchical graphene/CNFs/MnO_2 composite (with the dimension >1 cm), where primary structure (with a dimension of 100 μm) is made by the graphene networks, secondary structure (with a dimension of 1 μm) is made by the CVD grown-CNF forest on graphene skeletons, and tertiary structure (with a dimension of 10 nm) is made by a hemicylindrical MnO_2 nanosheetlike shell. Moreover, this 3D micro/nanointerconnected structure can provide uninterrupted charges transfer pathways in storage reaction.

layer formation and charge-transfer reactions; (2) conductive structural interconnectivity, which can provide both nanoporous channels for low-resistant ion diffusion and nanosized skeletons for electron transfer. However, those nanosized carbon materials are usually powderlike, and two inherent drawbacks cannot be avoided during the process of mixing them with some binders or additives to form a paste on the collectors:[28] (i) the disruption of long-range electron-conducting pathways in mixture of powdered components and the frustration of electrolyte infiltration to the interior surfaces by poorly interconnected macro-sized void volume and (ii) the aggregation and obscuration of nanosized 3D structured carbon powder when mixed with binding additives. Undoubtedly, these drawbacks will hinder their potential applications of nanosized electrode materials in supercapacitors, especially in flexible ones.

More recently, graphene-based microsized 3D structures have been proposed as a new class of ultralight and porous carbon bulk electrode materials due to their continuously robust interconnected macroporous skeletons, low mass density, and high electrical conductivity.[15,16] These 3D structures can serve as freestanding bulk electrode or collector for supercapacitors without extra binders or conductive additives compared with the previously reported 3D nanosized carbon materials.[29−31] Moreover, the macropores in these 3D structures can provide ion-buffering reservoirs to minimize the diffusion distances from the electrolyte to the interior surfaces, meanwhile the microsized and robust carbon skeletons in them can maintain long-range electron-conducting pathways.[11] However, in most cases, those freestanding collectors or electrodes have often suffered from the limited efficiency of mass transport and charge storage due to the limited SSA and the lack of nanosized pores. To solve these problems, a more design-rich strategy was proposed to integrate nanosized 3D structure into microsized 3D graphene bulk structure.[32−34] This design can not only enlarge SSA by providing mesopores and/or micropores but also show a synergistic enhancement effect by introducing both microsized 3D graphene structures and nanosized 3D structures in bulk electrode. It is demonstrated that this kind of 3D micro/nanosized carbon structures exhibits a superior electrochemical performance than those of the reported single 3D microsized or nanosized carbon structures. However, their mechanical properties and charge (electron and ion) transfer in storage reaction are still limited due to the lack of effective conjunction between micro- and nanostructures. It is suggested that this conjunction not only should be strong mechanical strength for keeping micro/nanostructure during bending operations but also provide interconnected pores and wall leading to uninterrupted electron-conducting and ion-diffusing pathways.

Herein, we present a design for fabricating a freestanding, lightweight, flexible, and mechanically robust 3D micro/nanointerconnected structure for supercapacitor electrodes based on the synergistic effects among the 3D graphene networks, CNFs forest, and MnO_2 nanosheets decorated on their surface (Figure 1). This type of highly flexible 3D microsized graphene networks produced by chemical vapor deposition (CVD) using pressed Ni foam as 3D template and catalyst can serve as current collector in the flexible supercapacitors. Moreover, the ion-buffering reservoirs resulted from those macropores (with a dimension of 100 μm) can minimize the diffusion distances from the electrolyte to the interior surfaces. On the other hand, CNF forest (with a dimension of 1 μm) directly grown on the flexible graphene skeletons by CVD can achieve a very tight conjunction between graphene and CNFs, and this type of hierarchical structure can provide an efficient transfer of electrons to each CNF in the forest. Simultaneously, the void volume between the neighboring CNFs can allow easy penetration of the electrolyte, further shortening the ion transfer pathway to their surface. Finally, to achieve a high capacitance, MnO_2 nanosheet as an active material was intimately coated on each CNF by the redox reaction between CNFs and $KMnO_4$ through microwave heating. Therefore, this rationally designed 3D micro/nanointerconnected structure, which combined micro- and nanostructured wall and/or pores seamlessly, can serve as the uninterrupted double charge freeway networks for quick electron transfer and easy electrolyte ion diffusion in the flexible bulk electrodes.

dx.doi.org/10.1021/am403760h | ACS Appl. Mater. Interfaces 2014, 6, 210−218

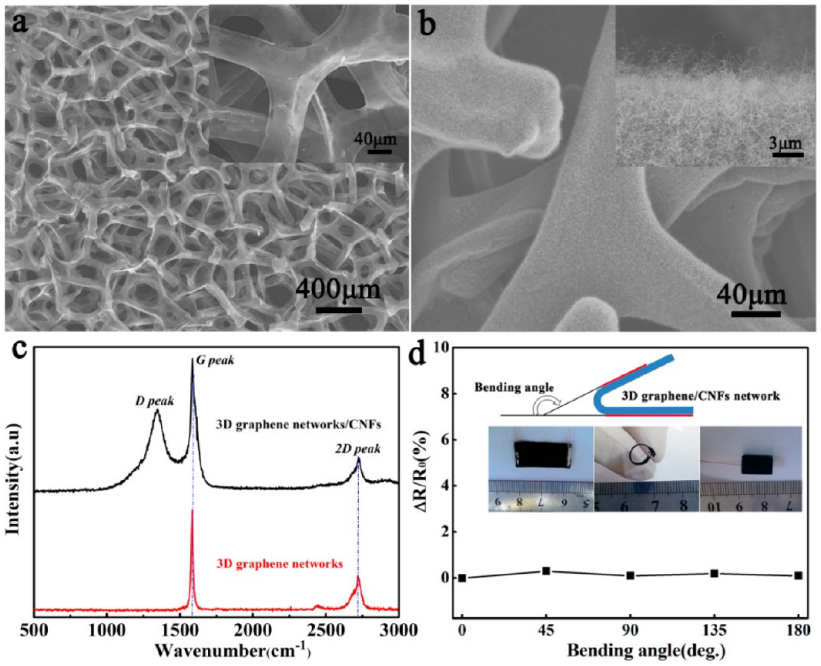

Figure 2. SEM images of 3D graphene networks after removal of Ni foam (a) and 3D graphene/CNF composite networks (b). The corresponding insets show high-magnification SEM images of both the graphene skeletons and CNF forest. (c) Raman spectra of 3D graphene networks and 3D graphene/CNFs composite networks. (d) Electrical resistance for 3D graphene/CNF networks at the different bending angles. The inset shows the digital photographs of the 3D graphene/CNF networks with different bending shapes.

RESULTS AND DISCUSSION

The morphologies of 3D graphene networks and 3D graphene/CNFs composite networks were observed by scanning electron microscopy (SEM) as shown in Figure 2a and b, respectively. After removal of Ni template, it can be seen that the graphene network skeleton has inherited the 3D porous structure from the pressed Ni foam without cracking and collapsing. And these 3D porous graphene networks would exhibit a high electrical conductivity of 55 S/cm and a large specific surface area of 392 m^2/g, which was reported in our previous work.[29] Moreover, the surface of the graphene skeleton is very smooth due to a conformal CVD growth on the Ni foam (the inset of Figure 2a). Subsequently, CNF forest was grown in a CVD system using graphene networks as the 3D catalyst support, and the obtained 3D graphene/CNT networks possess a lightweight density of 1.5−2.0 mg/cm^2 and a thickness less than 200 μm. As shown in Figure 2b, the as-grown CNF forest is dense and uniform around the whole graphene skeletons. The thickness of the CNF layer is estimated to be 6−10 μm by the width increase of the graphene skeleton (the inset of Figure 2b) and the average diameter of the as grown CNFs is around 20 nm, which was roughly measured from the high magnification SEM image (Supporting Information Figure S1). The structures of both 3D graphene networks and 3D graphene/CNFs composite networks were further determined by Raman spectroscopy, as shown in Figure 2c. The type Raman characteristics of the G peak at 1581 cm^{-1}, the 2D peak at 2713 cm^{-1}, and their peak intensity ratio (G/2D ratio) from the 3D graphene networks indicate those graphene networks comprised few-layer graphene sheets. And no D band is observed at 1360 cm^{-1}, implying the high quality of the as-grown structures. In comparison, the presence of the intense D band centered around 1360 cm^{-1} for the 3D graphene/CNFs networks can be associated with characteristic defects within the as-grown CNFs.

Figures 2d shows that the dependence of electrical-resistance variation as a function of the bending angles (from 0° to 180°) imposed on the 3D graphene/CNF networks. Inspiringly, there are little changes (less than 1%) occurring in the electrical resistance under different degrees of mechanical deformation. Simultaneously, it can be seen from the inset of Figure 2d that, after the growth of CNFs on the surface of 3D graphene network skeletons, the obtained freestanding 3D graphene/CNFs networks still maintain a high flexibility and superior mechanical strength properties the same as the 3D graphene networks.[29] These high flexible performances for graphene/CNFs composite might be mainly attributed to the following two factors: (1) the forestlike CNF structure is highly flexible and robust; (2) a direct growth of CNFs on the graphene skeletons allows excellent physical connectivity, as well as good electrical connectivity. Thus, this designed 3D grapheme/CNFs composite will make the fabrication of supercapacitor electrodes without additional carbon additives and polymeric binders. And, they can directly serve as freestanding flexible electrodes as well as an ideal support for active materials.

In order to achieve a high capacitance, a more design-rich strategy is to uniformly load well-dispersed active material on each CNF. However, CVD-grown CNF forest is usually hydrophobic owing to a lack of hydrophilic groups on the surface (Supporting Information Figure S2), resulting in hard access for the reaction solution to the inner of CNF forest. Preliminary results show that this type of 3D graphene/CNFs composite structures would inevitably suffer from the structural damages and become frangible and poorly flexible after the treatments of heating reflux in nitric and/or sulfuric acid, although its hydrophilic property can be improved. To solve this problem, the active material of MnO_2 was loaded by a redox reaction between carbon and $KMnO_4$ with microwave heating. Figure 3a and b shows no collapses of CNFs and agglomerations of MnO_2 in the composite with a MnO_2 mass

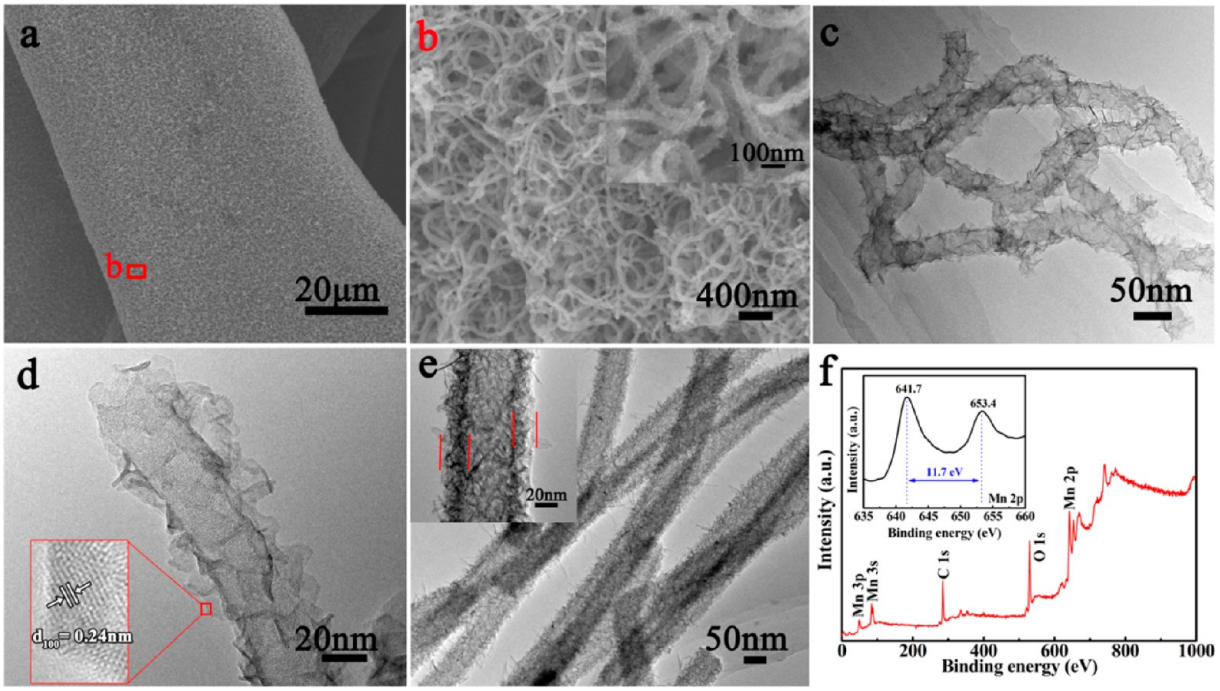

Figure 3. (a) SEM image of the graphene/CNFs/MnO_2 composite with an areal MnO_2 mass density of 0.1 mg/cm^2. (b) SEM image of the CNFs/MnO_2 composite forest marked by a red square in part a. The inset is the high-magnification SEM image. (c and d) Low- and high-magnification TEM images of CNFs/MnO_2 composite with the areal mass density of 0.1 mg/cm^2. The inset of d shows a lattice-resolution TEM image of the MnO_2 nanosheets marked by a red square. (e) Low-magnification TEM images of graphene/CNFs/MnO_2 composite with the areal mass density of 1.03 mg/cm^2. The inset shows its high-magnification TEM images and the MnO_2 shell are marked by red lines. (f) XPS survey spectra of graphene/CNFs/MnO_2 composite. The inset illustrates the narrow spectra of Mn2p peaks of the composite.

loading of 0.1 mg/cm^2, maintaining a micro/nanointerconnected structure. Moreover, it can be seen in the inset of Figure 3b that the nanostructured MnO_2 has been uniformly coated on the surface of each CNF, and the deposited MnO_2 layer consists of abundant nanosheets. This uniform coating of MnO_2 should be attributed to a self-limiting deposition during the redox reaction between $KMnO_4$ and the carbon from CNFs, in which the formed MnO_2 will cover the whole surface of CNFs and hinder the further redox reaction between them. On the other hand, CNFs serve as a sacrificial reductant substrate and convert aqueous permanganate to insoluble MnO_2, which will result in intimate contacts between MnO_2 and CNF for a fast electron collection and a robust mechanical connection.[35]

Further characterization of microstructures of 3D graphene/CNFs/MnO_2 composite was conducted on a high revolution transmission electron microscopy. As shown in Figure 3c, the layer-structured MnO_2 is ultrathin and well-dispersed on the CNFs. This morphology might be attributed to the merits of microwave heating,[36,37] such as high penetration depth, less thermal gradient in the reaction medium, and accordingly enhanced nucleation rate during the synthesis process. The crystalline MnO_2 nanosheets were also examined as shown in Figure 3d, indicating a 0.24 nm lattice spacing of the (100) planes of MnO_2 nanosheets. Moreover, it was found that, as the content of $KMnO_4$ increases, the MnO_2 nanosheet layer coating will become dense, but no aggregation of MnO_2 yet appears as shown in Supporting Information Figure S3. In our case, a relatively thick coating of MnO_2 with an areal mass density of 1.03 mg/cm^2 was achieved at 8 mg/mL of $KMnO_4$. From Figure 3e and its inset, it can be seen that and the deposited MnO_2 shell is about 20 nm in thickness and still layer-structured. Thus, this type of unique core−shell nanostructure would provide open nanoscale void to minimize ion diffusion length. In addition, X-ray photoelectron spectroscopy (XPS) was further employed to check our designed 3D graphene/CNFs/MnO_2 composite, as shown in Figure 3f. It was found that only signals from Mn, C, and O elements are detected. The binding energies of Mn 2p3/2 and Mn 2p1/2 (the inset of Figure 3f) are centered around 641.7 and 653.4 eV, revealing a difference of 11.7 eV in binding energy. This results is consistent with both the binding energy of Mn 2p3/2 and Mn 2p1/2 and the spin energy difference in MnO_2.[36]

To evaluate the electrochemical properties of our designed 3D micro/nanointerconnected structured electrodes, cyclic voltammetry (CV) and galvanostatic charge−discharge (GCD) measurements were performed on 3D graphene/CNFs/MnO_2 composite networks in 1 M Na_2SO_4 aqueous solution. During the measurements, we employed a three-electrode system, with the freestanding graphene/CNFs/MnO_2 composite networks, a Pt plate, and an Ag/AgCl (4 M KCl) electrode as the working, counter, and reference electrodes, respectively. These composite networks were directly fixed on the metal clip without metal support or current collectors used in the tests. Figure 4a shows the CV performance response to the scan rates. The areal mass density of MnO_2 in the samples kept the same as 0.1 mg/cm^2. It can be seen that the CV shapes are almost rectangular at scan rates below 400 mV/s and remain quasi-rectangular even at 1000 mV/s, indicating the superior charge storage performance and ultrafast response of the electrodes. Simultaneously, GCD tests were also carried out under different current densities in the voltage window from 0 to 1 V, as shown in Figure 4b. It was demonstrated that all the charging curves are symmetric to their corresponding discharge

dx.doi.org/10.1021/am403760h | ACS Appl. Mater. Interfaces 2014, 6, 210−218

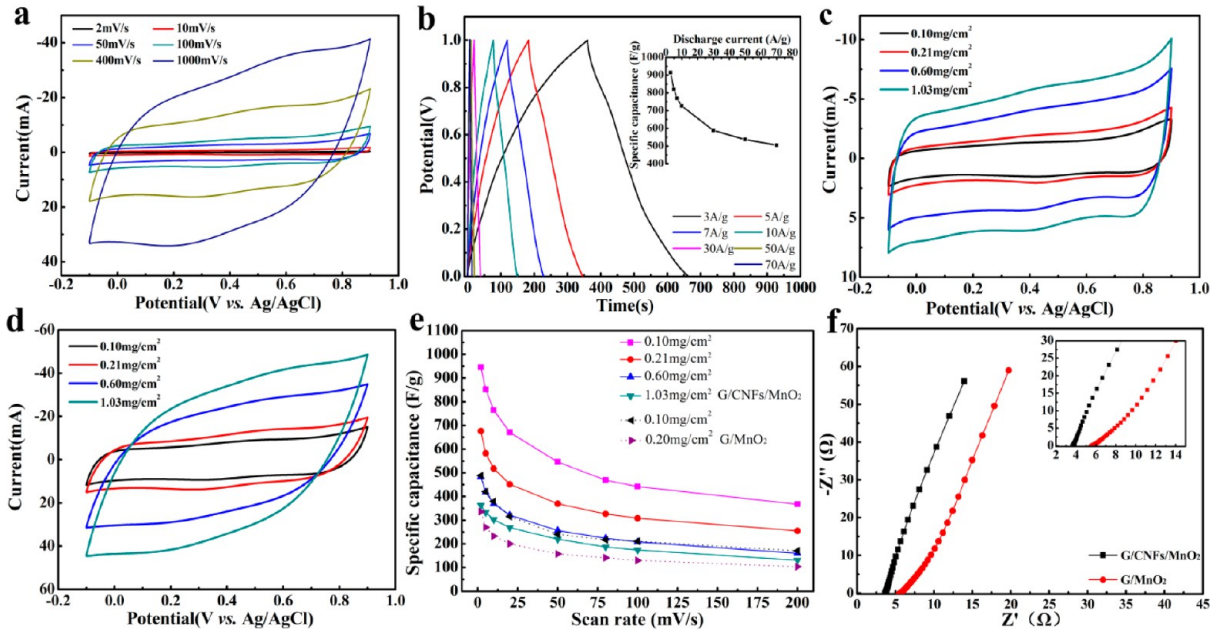

Figure 4. (a) CVs of a 3D graphene/CNFs/MnO_2 composite electrode with a fixed areal mass density of 0.1 mg/cm^2 at different scan rates. (b) GCD curves of a 3D graphene/CNFs/MnO_2 composite electrode with a fixed areal mass density of 0.1 mg/cm^2 at different current densities. (inset) Specific capacitance vs current density for 0.1 mg/cm^2 of MnO_2 from GCD curves. (c and d) CVs of graphene/CNFs/MnO_2 composite electrodes with different areal mass densities of MnO_2 at scan rates of 20 (c) and 200 mV/s (d). (e) Specific capacitance vs scan rate for samples with different areal mass densities of MnO_2 calculated from CVs. (f) Nyquist plots of the graphene/CNFs/MnO_2 composite electrode and graphene/MnO_2 composite electrode with a fixed MnO_2 mass loadings of 0.1 mg/cm^2, respectively.

counterparts and show good linear voltage−time profiles. These results indicate a good capacitive behavior of the designed 3D micro/nanointerconnected structure. In addition, the inset of Figure 4b shows the specific capacitances as a function of different current densities from 3 to 70 A/g, and the maximum value of the specific capacitance was estimated to be 920 F/g.

The CV performance response to the areal mass densities of MnO_2 have been further estimated in Figures 4 c and d, at scan rates of 20 and 200 mV/s, respectively. The corresponding current increases with increased MnO_2 content in the electrodes for both scan rates, indicating more materials contribute to charge storage. As the scan rate increases from 20 to 200 mV/s, the CV shapes remain nearly rectangular except only a few deviations as the MnO_2 coating gets thicker. These results further indicate the excellent electrochemical performance of this kind of 3D graphene/CNFs/MnO_2 composite networks. Moreover, the specific capacitances according to the mass of MnO_2 have been derived from CVs and plotted in Figure 4e. Here, to evaluate the specific capacitance of MnO_2, the plot was processed by subtracting the base charge of the bare 3D graphene/CNFs networks, of which the value is very small due to lack of electroactive sites and hydrophilic groups. The specific capacitance of 946 F/g (for 0.1 mg/cm^2 MnO_2 loading) and 676 F/g (for 0.21 mg/cm^2 MnO_2 loading) can be obtained at a scan rate of 2 mV/s. In contrast, an electrode made from a freestanding 3D graphene/MnO_2 composite networks with a similar areal density shows a much lower specific capacitance (482 and 336 F/g for 0.11 and 0.20 mg/cm^2 MnO_2 loading, respectively). It is believed that such a large difference is caused by the incorporation of nanosized 3D structure of CNF forest, which is the key reason for obtaining high performance in our tests. Thus, it is proposed that CNF forest would provide an electrochemical transition region between 3D graphene networks and nanostructured MnO_2 layer. In this region, a double highway for electron transfer to the collector and electrolyte ions access to MnO_2 surfaces are formed by CNFs and their open voids in the forest, respectively. Simultaneously, the extended large active surface area of CNF forest allows a thinnest MnO_2 layer, and consequently these composite networks can achieve a high specific surface area, as shown in Supporting Information Table S1.

For a deep understanding of the designed 3D micro/nanointerconnected structure, the Nyquist plot of the graphene/CNFs/MnO_2 composite electrode in the frequency range from 0.1 Hz to 100 kHz at open-circuit voltage with an ac amplitude of 5 mV was obtained in a 1 M Na_2SO_4 aqueous solution, as shown in Figure 4f. In the Nyquist plot, the intercept at the real part (Z′) reflects the combination of the ionic resistance of the electrolyte and the electrode resistance of the freestanding graphene/CNFs/MnO_2 composite. The ionic resistance of the electrolyte is ∼3.1 Ω, which was measured using Pt wire as the working electrode in the same test system. After subtracting the ionic resistance of the electrolyte from the value of Z′, the resistances of graphene/CNFs/MnO_2 composite and graphene/MnO_2 composite electrodes were 0.6 and 2.5 Ω for 0.1 mg/cm^2 MnO_2 mass loading, respectively. These values suggest good contacts among nanostructured MnO_2, CNFs, and 3D graphene networks. While, this rather larger resistance of graphene/MnO_2 composite electrode should be mainly attributed to its thicker MnO_2 layer.

After systematically checked the electrochemical performances of as-prepared electrode materials, we have further assembled those 3D micro/nanointerconnected structures into an ultralight flexible asymmetric supercapacitor, in which the 3D graphene/CNFs/MnO_2 composite networks was employed as the positive electrode and graphene/active carbon (AC)

dx.doi.org/10.1021/am403760h | ACS Appl. Mater. Interfaces 2014, 6, 210−218

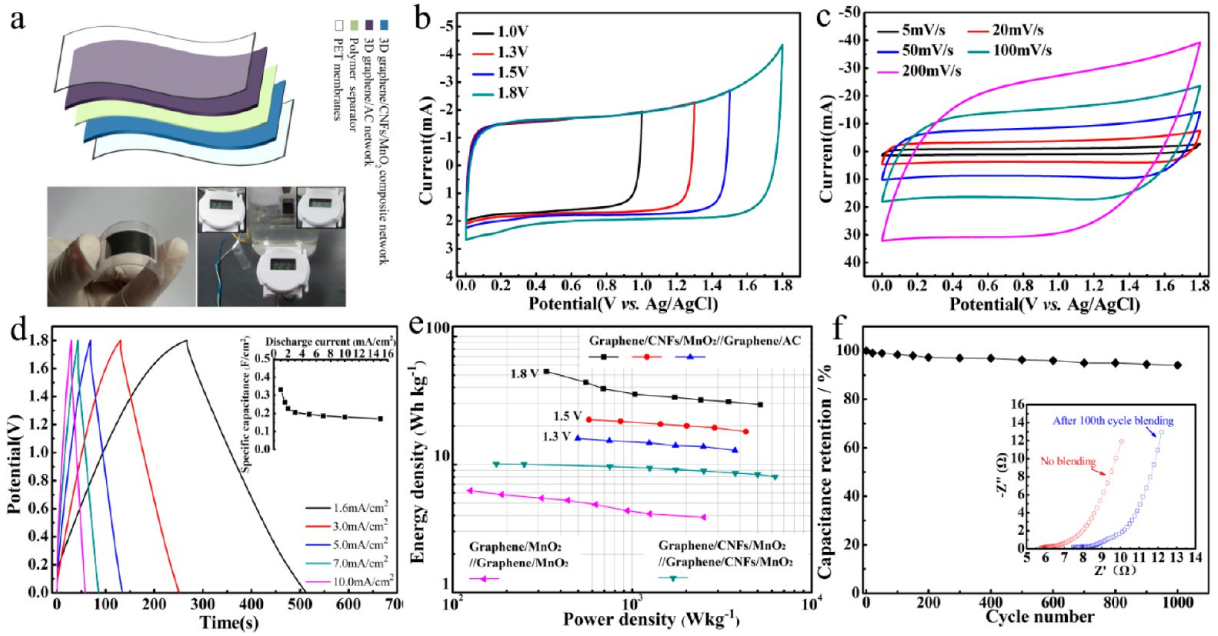

Figure 5. (a) Schematic structure of the flexible supercapacitor consisting of a polymer separator, two PET membranes, and two asymmetric graphene-based electrodes, of which graphene/CNFs/MnO_2 composite networks was used as the positive electrode and graphene/AC networks as the negative electrode. The left bottom digital photograph shows the flexibility of the device during bending operations. The right bottom digital photograph shows a digital clock driven by the flexible supercapacitor. (b) CV curves of an optimized 3D graphene/CNFs/MnO_2 composite network‖3D graphene/AC network asymmetric flexible supercapacitor measured at different potential windows in 1 M Na_2SO_4 aqueous solution at a scan rate of 10 mV/s. (c) CVs of the flexible supercapacitor at scan rates of 5, 20, 50, 100, and 200 mV/s. (d) GCD curves of the flexible asymmetric supercapacitor at different current densities. (inset) Areal capacitance vs current density. (e) Ragone plot related to energy and power densities of the designed asymmetric flexible supercapacitor with various voltage windows, the designed symmetric flexible supercapacitor, and another symmetric flexible supercapacitor based on 3D graphene/MnO_2 composite networks. (f) Cycling performance of the flexible supercapacitor for charging and discharging at a current density of 10 mA/cm^2. The inset shows the Nyquist plots of the flexible supercapacitor without blending and after 100th cycle blending at a bending angle of 90°.

networks as the negative electrode. These two electrodes, separated by a polymer membrane, were sandwiched between polyethylene terephthalate (PET) films and immersed in 1 M Na_2SO_4 solution, as shown in Figure 5a. The as-fabricated supercapacitor was lightweight (~12 mg/cm^2), thin (~0.8 mm), and highly flexible (the left bottom of Figure 5a). Inspiringly, this designed supercapacitor, after charging at 3 mA/cm^2 for 2 min, could drive a digital clock and lasts for a long time up to 42 min (the right bottom of Figure 5a). This result reveals the potential application of the fabricated ultralight flexible supercapacitor in flexible and lightweight energy storage. At the same time, the cell voltage of the asymmetric device was ensured by a pre-experiment of CV measurements in a three-electrode system separately on 3D graphene/CNFs/MnO_2 composite networks with a 1.0 mg/cm^2 MnO_2 mass loading and graphene/AC networks with a 1.6 mg/cm^2 AC mass loading (Supporting Information Figure S4). The 3D graphene/CNFs/MnO_2 composite network was measured within a stable potential window of −0.1−0.9 V (vs Ag/AgCl), while the graphene/AC networks was measured within a potential window of −1.0 to 0 V (vs Ag/AgCl) at a scan rate of 10 mV/s. Considering the total voltage of asymmetric supercapacitor can be expressed as the sum of the potential range for both electrodes, it is deduced that the cell voltage can be extended up to 1.8 V in 1 M Na_2SO_4 aqueous solution for an asymmetric supercapacitor.

Figure 5b shows the CV responses of an optimized asymmetric supercapacitor to applied window potentials at a scan rate of 10 mV/s. It can be seen that the as-fabricated cell shows an ideal capacitive behavior with rectangle CV curves even at the window potential up to 1.8 V. Moreover, it is was further confirmed from Figure 5c that those CV curves exhibit rectangularlike shapes without obvious redox peaks with the increasing scan rates, even up to 200 mV/s. This result can be ascribed to the fast surface electrosorption of Na^+ cations and the subsequent quick reversible faradic process that occurs between Na^+ cations and MnO_2. In addition, to demonstrate the flexibility of the supercapacitor, CV curves were measured under different curvatures of 0°, 45°, 90°, and 180° at a scan rate of 20 mV/s (Supporting Information Figure S5). No significant change of their electrochemical performance under bending conditions was observed, which suggests the great potential application of flexible storage devices.

Furthermore, GCD curves of the ultralight flexible asymmetric supercapacitor were also explored at various current densities over the voltage window of 0−1.8 V, as shown in Figure 5d. Both the linear profiles of charge and discharge curves and their symmetry demonstrate the good capacitive characteristics of the asymmetric supercapacitor. The areal capacitances with respect to current densities have been derived from the GCDs and plotted in the inset of Figure 5d. The maximum value is achieved to be 0.33 F/cm^2 at current density of 1 mA/cm^2 and preserves 51% of its areal capacitance when the current density increases up to 15 mA/cm^2. To further evaluate the electrochemical performance of the 3D graphene/CNFs/MnO_2 composite network‖3D graphene/AC network ultralight flexible supercapacitor, Ragone plots relating energy and power densities was calculated in a voltage window

dx.doi.org/10.1021/am403760h | ACS Appl. Mater. Interfaces 2014, 6, 210−218

of 0−1.3, 0−1.5, and 0−1.8 V with current densities from 1 to 15 mA/cm^2 (Figure 5e). With an operating potential of 1.8 V, the maximum energy density of the asymmetric supercapacitors reaches 53.4 Wh/kg with a power density of 332.5 kW/kg. This maximum energy density is much higher than those of other MnO_2-based asymmetric supercapacitors with aqueous electrolyte solutions, such as MnO_2/graphene composite (MGC)||graphene (30.4 Wh/kg),[38] 3D graphene/MnO_2 composite||3D graphene (44 Wh/kg),[39] 3D graphene||MnO_2 (23.2 Wh/kg),[40] MnO_2||AC (7.0−28.8 Wh/kg),[41−46] CNTs/MnO_2||CNTs/SnO_2 (20.3 Wh/kg),[47] $NaMnO_2$||AC (19.5 Wh/kg),[48] MnO_2||Fe_3O_4 (8.1 Wh/kg),[43] MnO_2||FeOOH (12 Wh/kg),[49] MnO_2||polypyrrole (7.37 Wh/kg),[50] MnO_2||polyaniline (5.86 Wh/kg),[50] and MnO_2||poly(3,4-ethylenedioxythiophene) (13.5 W h/kg).[50] Moreover, this assembled asymmetric supercapacitor can also exhibit a good power characteristic of supercapacitor, and the power density can reach 5172.4 W/kg when the energy density keeps at 29.4 W h/kg in a voltage window of 0−1.8 V. It is indicated that the power density obtained in our cases can not only meet the requirements as power supply components in hybrid vehicle systems (PNGV, 15 kW/kg)[11] but also extends further smart applicability in flexible and lightweight energy supply systems. In addition, it is worth noting that, to some extent, the applied energy/power densities of the supercapacitors can be well adjusted by selecting a suitable window voltage to meet practical requirements (Figure 5e).

For comparison, two symmetric flexible supercapacitors were also fabricated based on 3D graphene/CNFs/MnO_2 composite networks and 3D graphene/MnO_2 composite networks, respectively, and were tested galvanostatically between 0 and 1.0 V. The symmetric supercapacitor made from 3D graphene/CNFs/MnO_2 composite networks exhibits a maximum energy density of 10.1 W h/kg (with a power density of 175 kW/kg), which are superior to that of the symmetric supercapacitor made from 3D graphene/MnO_2 composite networks (6.2 W h/kg and 125 kW/kg) as well as other symmetrical supercapacitors such as doped 3D graphene||3D graphene (8.7 W h/kg),[30] MnO_2/graphene composite (MGC)||MGC (5.2 W h/kg),[38] graphene||graphene (2.8 W h/kg),[38] and MnO_2||MnO_2 supercapacitors within a cell voltage of 0.6−1.0 V (1.9−3.3 W h/kg).[43,50,51] A rough comparison demonstrates that these values are much higher than those of other symmetric and asymmetric flexible supercapacitors, of which the energy densities and the electrode materials are listed in Supporting Information Table S2. Meanwhile, both the leakage current and the self-discharge of as-fabricated symmetrical device were also tested, as shown in Supporting Information Figure S6. It can be seen that the leakage current was stable at about 22.8 μA/g for a long time beyond 2 h, and the output voltage of the device reached about 0.21 V after 24 h. It is suspected that these large leakage current and self-discharge characteristics may result from the cooperation from the high mobility of Na^+ ion in liquid electrolyte and their easy penetrability into the macroporous separator. Meanwhile, these electrochemical performances could be significantly improved by using solid-state electrolyte design such as H_2SO_4[−52] or H_3PO_4[−53] PVA gel electrolyte. Further research is still underway.

In addition, long cycling life is one of the most critical factors of flexible supercapacitors in real applications. The cycling stability of our designed asymmetric supercapacitor was tested at a constant current density of 10 mA/cm^2 for 1000 cycles. Figure 5f shows the capacitance retention ratio of the asymmetric supercapacitor charged at 1.8 V as a function of the cycle number. It is observed that only a slight capacitance loss occurs after 100 cycles, and the Coulombic efficiency remains above 98.4%. After 1000 cycles, the asymmetric supercapacitor still exhibits excellent capacitive performance with only 5.9% degradation of the initial specific capacitance. This retention of 94.1% after 1000 cycles of the designed asymmetric supercapacitor is comparable to those of other reported asymmetric supercapacitors such as MGC||graphene (79% retention after 1000 cycles),[38] MGC||CNTs (95% retention after 5000 cycles),[54] MGC||activated CNFs (97.3% retention after 1000 cycles),[22] and MGC/functionalized CNTs||AC/functionalized CNTs (95% retention after 2000 cycles).[55] Moreover, the bending cycle stability of the flexible supercapacitor (bending angle of 90°) was also tested by electrochemical impedance spectroscopy (EIS), as shown in the inset of Figure 5f. After the 100th bending, due to a small mechanical damage to this micro/nanointerconnected structure electrode, the initial of resistance of the asymmetric supercapacitor slightly increases from 5.72 to 7.5 Ω, indicating its excellent mechanical and flexible properties. Thus, it is concluded that the high cycling performances and highly flexible properties should be due to the good contacts among graphene, CNFs, and MnO_2, which are formed by the direct growth of CNFs on 3D graphene networks and the subsequent redox deposition of MnO_2 on the surface of CNFs. Additionally, our research suggests that the redox deposition of MnO_2 can effectively avoid the material loss or film detachment from CNFs surfaces, which are common causes for limited cycling life of MnO_2-based supercapacitors.

CONCLUSIONS

In summary, we have developed a type of freestanding, lightweight, flexible, and mechanically robust 3D graphene/CNFs/MnO_2 composite networks, which can be used as electrodes of ultralight flexible supercapacitors. The obtained 3D micro/nanointerconnected flexible electrode exhibits outstanding electrochemical performances with high specific capacitance, remarkable energy density, and cycling performance. Their superior electrochemical and flexible performances can be attributed to the following aspects: (1) The interconnected macropores within 3D graphene networks can serve as ion-buffering reservoirs to minimize the diffusion length from the external electrolyte to the interior surfaces. Moreover, the open void volume in both CNF forest and their surface coated MnO_2 nanosheet layer can further enhance ion transport and charge storage capability. (2) The conductive CNFs-based nanosized 3D structure together with graphene-based microsized 3D networks can provide multidimensional electron pathways to accelerate its transport in the bulk electrodes. (3) The good connections among each component promise a freestanding robust mechanical and flexible electrode without use of binding actives and collector, as well as maintaining micro/nanostructured interconnected wall and pores leading to uninterrupted electron-conducting and ion-diffusing pathways. These outstanding electrochemical behaviors of the 3D graphene/CNFs/MnO_2 composite networks will make it be attractive for real applications in the ultralight flexible supercapacitors.

In our initial applications, the simple assembly of this ultralight flexible asymmetric and symmetric supercapacitors show excellent energy densities and capacitances. This indicates that the ultralight flexible supercapacitors fabricated in our case

should have great potential in hybrid vehicle systems, as well as lightweight and flexible energy supply systems for small flying devices, adhesive tape-like devices, wearable devices, and so on. And, it can be foreseen that this design concept would be readily applicable toward other active materials based on redox-based deposition with water-soluble oxidizing agent (such as FeO_4^{2-}, $RuO4^-$, and so on) on carbon materials for energy storage systems, which will bring new opportunities for a wide range of applications.

EXPERIMENTS AND METHODS

Growth of 3D Graphene/CNFs Networks. First, the flexible 3D graphene networks were grown by CVD with the pressed Ni foam as template and catalyst. After that, 0.2 g of $Co(NO_3)_2{\cdot}6H_2O$, 0.8 g of urea, and 0.05 g sodium dodecyl benzene sulfonate (SDBS) were dissolved in 180 mL of deionized water. Subsequently, the obtained 3D graphene networks with a size of 1 cm × 2 cm were immersed into 20 mL of the above $Co(NO_3)_2$ solution for 30 min to wet completely, and then, heated using a microwave oven (Haier, 2450 MHz, 700 W) for 5 min. After drying in air at 80 °C for 20 min, the resulting graphene foams were loaded into a quartz tube for the CVD growth of CNFs under flowing of a reactive gas mixture (C_2H_2: 5 SCCM, Ar: 100 SCCM, and H_2: 20 SCCM), using ethylene as the precursor. The chemical vapor reduction and deposition reaction were performed at 500 °C for 60 min before the furnace was cooled down gradually in Ar atmosphere to room temperature. Finally, the resulting 3D graphene/CNFs composite networks was soaked in 1 M HCl aqueous solution for 6 h to remove the Co catalyst.

Preparation of Graphene/CNFs/MnO_2 Composite Networks. MnO_2 nanosheet layer was uniformly coated onto CNF forest by redox reaction between CNF and $KMnO_4$ under microwave heating. The predetermined amount of $KMnO_4$ (Supporting Information Table S3) and SBDS (0.01g) were added into 50 mL of deionized water and stirred for 10 min. Then, the 3D graphene/CNFs networks were immersed in the above solution for 6 h to make $KMnO_4$ absorb on the walls of CNFs sufficiently. Subsequently, the resulting mixture was heated using the same microwave oven for 3 min, and then cooled to room temperature naturally. Finally, the graphene/CNFs/MnO_2 composite networks was taken out, washed with distilled water, and dried at 80 °C for 12 h in a vacuum oven. The mass of the deposited MnO_2 nanomaterials was calculated by the equation from the redox reaction ($4KMnO_4^- + 3C + H_2O = 4MnO_2 + CO_3^{2-} + 2HCO_3^-$):

$$\Delta m_{(MnO_2)} = 347.76\Delta m_{(\text{weight difference})}/311.76$$

where $\Delta m_{(\text{weight difference})}$ is the weight difference between the networks before coating and after postdrying. Additionally, the preparation of 3D graphene/MnO_2 composite networks was carried out in the same manner, where the 3D graphene networks was directly used as carbon source and freestanding substrate. And, the morphology of graphene/MnO_2 composite was shown in Supporting Information Figure S7.

Electrochemical Measurement. In half cell tests, a three-electrode system was employed to measure electrochemical performances, where 3D graphene/CNFs/MnO_2 composite networks, 3D graphene/MnO_2 composite networks, and 3D graphene/AC composite networks were used as working electrodes, Ag/AgCl as reference electrode, and Pt plate as counter electrode, respectively. Among them, 3D graphene/AC composite networks was prepared by dipping graphene networks into AC ink (mixing 85 wt % AC, 10 wt % acetylene black, and 5 wt % polyvinylidene fluoride binder dispersed in *N*-methyl-2-pyrrolidone solvent) and subjected to "dip and dry" coating cycles to control the mass loading of AC.[54] In full cell tests, the flexible supercapacitor devices were assembled as we previously reported.[29] In the device, the 3D graphene/CNFs/MnO_2 composite networks with a mass loading of 1.0 mg/cm^2 and 3D graphene/active carbon (AC) networks with a mass loading of 1.6 mg/cm^2 were used as positive electrode and negative electrode, respectively. The total thickness of as-fabricated devices were ∼0.8 mm, and their weight was less than 12 mg/cm^2. In the above measurements, 1 M Na_2SO_4 aqueous solution was used as the electrolyte and kept at pH 10.

Material Characterization. The materials characterization were conducted by transmission electron microscopy (TEM, FEI Tecnai F30), field emission scanning electron microscopy (FE-SEM, Hitachi S-4800), X-ray photoelectron spectroscope (XPS, PHI-5702) using Mg Ka X-ray ($h\nu$ = 1253.6 eV) as the excitation source, Raman spectroscopy (JY-HR800 micro-Raman, 532 nm), Brunauer–Emmett–Teller (BET ASAP 2020), microbalance (Mettler, XS105DU), and electrochemical workstation (RST5200, Zhengzhou Shiruisi Instrument Technology Co., Ltd., China).

ASSOCIATED CONTENT

Supporting Information

SEM images of 3D graphene/CNFs composite networks, 3D graphene/MnO_2 composite networks, and 3D graphene/CNFs/MnO_2 composite networks with different MnO_2 mass loadings, respectively; the contact angle for 3D graphene/CNFs composite networks; comparative CV curves for 3D graphene/CNFs/MnO_2 composite networks and 3D graphene/AC composite networks, and asymmetric supercapacitor at different curvatures; leakage current and self-discharge of the supercapacitor device. Tables for surface areas of 3D graphene/CNFs/MnO_2 composites, relationship of the amount of $KMnO_4$ and the resulting MnO_2 mass loading, and summary of energy densities of previous symmetric and asymmetric flexible supercapacitors based on MnO_2, CNTs, or/and graphene. This material is available free of charge via the Internet at http://pubs.acs.org.

AUTHOR INFORMATION

Corresponding Authors

*E-mail: heyongming11@163.com. Tel.: +86 (0) 931 891 2616. Fax: +86 (0) 931 891 3554.
*E-mail: xieeq@lzu.edu.cn.

Author Contributions

†Y.H. and W.C. contributed equally to this work.

Notes

The authors declare no competing financial interest.

ACKNOWLEDGMENTS

This work was financially supported by the National Natural Science Foundation of China (No. 61176058), partially by the Fundamental Research Funds for the Central Universities (lzujbky-2013-231), and the National Natural Science Foundation of China (No. 51202100).

REFERENCES

(1) Rogers, J. A.; Huang, Y. G. *Proc. Natl. Acad. Sci. U.S.A.* **2009**, *106*, 10875−10876.
(2) Lu, X.; Xia, Y. *Nat. Nanotechnol.* **2006**, *1*, 163−164.
(3) Nathan, A.; Ahnood, A.; Cole, M. T.; Sungsik, L.; Suzuki, Y.; Hiralal, P.; Bonaccorso, F.; Hasan, T.; Garcia-Gancedo, L.; Dyadyusha, A.; Haque, S.; Andrew, P.; Hofmann, S.; Moultrie, J.; Daping, C.; Flewitt, A. J.; Ferrari, A. C.; Kelly, M. J.; Robertson, J.; Amaratunga, G. A. J.; Milne, W. I. *Proc. IEEE* **2012**, *100*, 1486−1517.
(4) Nishide, H.; Oyaizu, K. *Science* **2008**, *319*, 737−738.
(5) Zhang, Y.; Feng, H.; Wu, X.; Wang, L.; Zhang, A.; Xia, T.; Dong, H.; Li, X.; Zhang, L. *Int. J. Hydrogen Energy* **2009**, *34*, 4889−4899.
(6) Simon, P.; Gogotsi, Y. *Nat. Mater.* **2008**, *7*, 845−854.
(7) Conway, B. E. *Electrochemical Supercapacitors: Scientific, Fundamentals and Technological Applications*; Plenum: New York, 1999; p 19−20.
(8) Zhang, L. L.; Zhao, X. S. *Chem. Soc. Rev.* **2009**, *38*, 2520−2531.
(9) Inagaki, M.; Konno, H.; Tanaike, O. *J. Power Sources* **2010**, *195*, 7880−7903.
(10) Pandolfo, A. G.; Hollenkamp, A. F. *J. Power Sources* **2006**, *157*, 11−27.
(11) Wang, D.-W.; Li, F.; Liu, M.; Lu, G. Q.; Cheng, H.-M. *Angew. Chem., Int. Ed.* **2008**, *47*, 373−376.
(12) Largeot, C.; Portet, C.; Chmiola, J.; Taberna, P.-L.; Gogotsi, Y.; Simon, P. *J. Am. Chem. Soc.* **2008**, *130*, 2730−2731.
(13) Merlet, C.; Rotenberg, B.; Madden, P. A.; Taberna, P.-L.; Simon, P.; Gogotsi, Y.; Salanne, M. *Nat. Mater.* **2012**, *11*, 306−310.
(14) Jiang, H.; Lee, P. S.; Li, C. *Energy Environ. Sci.* **2013**, *6*, 41−53.
(15) Li, C.; Shi, G. *Nanoscale* **2012**, *4*, 5549−5563.
(16) Nardecchia, S.; Carriazo, D.; Ferrer, M. L.; Gutierrez, M. C.; del Monte, F. *Chem. Soc. Rev.* **2013**, *42*, 794−830.
(17) Liu, R.; Duay, J.; Lee, S. B. *Chem. Commun.* **2011**, *47*, 1384−1404.
(18) Frackowiak, E.; Béguin, F. *Carbon* **2001**, *39*, 937−950.
(19) Chmiola, J.; Yushin, G.; Gogotsi, Y.; Portet, C.; Simon, P.; Taberna, P. L. *Science* **2006**, *313*, 1760−1763.
(20) Wang, Y. G.; Li, H. Q.; Xia, Y. Y. *Adv. Mater.* **2006**, *18*, 2619−2623.
(21) Lota, G.; Fic, K.; Frackowiak, E. *Energy Environ. Sci.* **2011**, *4*, 1592−1605.
(22) Fan, Z.; Yan, J.; Wei, T.; Zhi, L.; Ning, G.; Li, T.; Wei, F. *Adv. Funct. Mater.* **2011**, *21*, 2366−2375.
(23) Huang, Y.; Liang, J.; Chen, Y. *Small* **2012**, *8*, 1805−1834.
(24) Fan, Z.; Yan, J.; Zhi, L.; Zhang, Q.; Wei, T.; Feng, J.; Zhang, M.; Qian, W.; Wei, F. *Adv. Mater.* **2010**, *22*, 3723−3728.
(25) Fan, Z.-J.; Yan, J.; Wei, T.; Ning, G.-Q.; Zhi, L.-J.; Liu, J.-C.; Cao, D.-X.; Wang, G.-L.; Wei, F. *ACS Nano* **2011**, *5*, 2787−2794.
(26) Du, F.; Yu, D.; Dai, L.; Ganguli, S.; Varshney, V.; Roy, A. K. *Chem. Mater.* **2011**, *23*, 4810−4816.
(27) Zhao, X.; Sanchez, B. M.; Dobson, P. J.; Grant, P. S. *Nanoscale* **2011**, *3*, 839−855.
(28) Sassin, M. B.; Chervin, C. N.; Rolison, D. R.; Long, J. W. *Acc. Chem. Res.* **2013**, *46*, 1062−1074.
(29) He, Y.; Chen, W.; Li, X.; Zhang, Z.; Fu, J.; Zhao, C.; Xie, E. *ACS Nano* **2012**, *7*, 174−182.
(30) Wu, Z.-S.; Winter, A.; Chen, L.; Sun, Y.; Turchanin, A.; Feng, X.; Müllen, K. *Adv. Mater.* **2012**, *24*, 5130−5135.
(31) Niu, Z.; Chen, J.; Hng, H. H.; Ma, J.; Chen, X. *Adv. Mater.* **2012**, *24*, 4144−4150.
(32) Wu, Z.-S.; Sun, Y.; Tan, Y.-Z.; Yang, S.; Feng, X.; Müllen, K. *J. Am. Chem. Soc.* **2012**, *134*, 19532−19535.
(33) Dong, X.; Ma, Y.; Zhu, G.; Huang, Y.; Wang, J.; Chan-Park, M. B.; Wang, L.; Huang, W.; Chen, P. *J. Mater. Chem.* **2012**, *22*, 17044−17048.
(34) Wang, W.; Guo, S.; Bozhilov, K. N.; Yan, D.; Ozkan, M.; Ozkan, C. S. *Small* **2013**, *9*, 3714−3721.
(35) Jin, X.; Zhou, W.; Zhang, S.; Chen, G. Z. *Small* **2007**, *3*, 1513−1517.
(36) Yan, J.; Fan, Z.; Wei, T.; Qian, W.; Zhang, M.; Wei, F. *Carbon* **2010**, *48*, 3825−3833.
(37) Meher, S. K.; Rao, G. R. *J. Power Sources* **2012**, *215*, 317−328.
(38) Wu, Z.-S.; Ren, W.; Wang, D.-W.; Li, F.; Liu, B.; Cheng, H.-M. *ACS Nano* **2010**, *4*, 5835−5842.
(39) Choi, B. G.; Yang, M.; Hong, W. H.; Choi, J. W.; Huh, Y. S. *ACS Nano* **2012**, *6*, 4020−4028.
(40) Gao, H.; Xiao, F.; Ching, C. B.; Duan, H. *ACS Appl. Mater. Interfaces* **2012**, *4*, 2801−2810.
(41) Hong, M. S.; Lee, S. H.; Kim, S. W. *Electrochem. Solid-State Lett.* **2002**, *5*, A227−A230.
(42) Xu, C.; Du, H.; Li, B.; Kang, F.; Zeng, Y. *J. Electrochem. Soc.* **2009**, *156*, A435−A441.
(43) Cottineau, T.; Toupin, M.; Delahaye, T.; Brousse, T.; Bélanger, D. *Appl. Phys. A: Mater. Sci. Process.* **2006**, *82*, 599−606.
(44) Brousse, T.; Toupin, M.; Bélanger, D. *J. Electrochem. Soc.* **2004**, *151*, A614−A622.
(45) Yuan, A.; Zhang, Q. *Electrochem. Commun.* **2006**, *8*, 1173−1178.
(46) Brousse, T.; Taberna, P.-L.; Crosnier, O.; Dugas, R.; Guillemet, P.; Scudeller, Y.; Zhou, Y.; Favier, F.; Bélanger, D.; Simon, P. *J. Power Sources* **2007**, *173*, 633−641.
(47) Yu, C.; Masarapu, C.; Rong, J.; Wei, B.; Jiang, H. *Adv. Mater.* **2009**, *21*, 4793−4797.
(48) Qu, Q. T.; Shi, Y.; Tian, S.; Chen, Y. H.; Wu, Y. P.; Holze, R. *J. Power Sources* **2009**, *194*, 1222−1225.
(49) Jin, W.-H.; Cao, G.-T.; Sun, J.-Y. *J. Power Sources* **2008**, *175*, 686−691.
(50) Khomenko, V.; Raymundo-Piñero, E.; Frackowiak, E.; Béguin, F. *Appl. Phys. A: Mater. Sci. Process.* **2006**, *82*, 567−573.
(51) Khomenko, V.; Raymundo-Piñero, E.; Béguin, F. *J. Power Sources* **2006**, *153*, 183−190.
(52) Meng, C.; Liu, C.; Chen, L.; Hu, C.; Fan, S. *Nano Lett.* **2010**, *10*, 4025−4031.
(53) Yuan, L.; Lu, X.-H.; Xiao, X.; Zhai, T.; Dai, J.; Zhang, F.; Hu, B.; Wang, X.; Gong, L.; Chen, J.; Hu, C.; Tong, Y.; Zhou, J.; Wang, Z. L. *ACS Nano* **2011**, *6*, 656−661.
(54) Yu, G.; Hu, L.; Vosgueritchian, M.; Wang, H.; Xie, X.; McDonough, J. R.; Cui, X.; Cui, Y.; Bao, Z. *Nano Lett.* **2011**, *11*, 2905−2911.
(55) Cheng, Y.; Zhang, H.; Lu, S.; Varanasi, C. V.; Liu, J. *Nanoscale* **2013**, *5*, 1067−1073.